http://journal.uir.ac.id/index.php/JGEET

E-ISSN : 2541-5794
P-ISSN : 2503-216X

Journal of Geoscience,
Engineering, Environment, and Technology
Vol xx No xx 20xx

RESEARCH ARTICLE

Quantifying the Effect of Natural Consolidation and Fluid Discharge on Land Subsidence of the Sidoarjo Mud Volcano, East Java, Indonesia

Giri Bayuaji [1], Asep Saepuloh [1,*], Astyka Pamumpuni [1,*], Dedy Wijnarko [2], Santika Tristi Maryudhaningrum [3]

[1] *Faculty of Earth Sciences and Technology, Bandung Institute of Technology, Jl. Ganesha No. 10, Bandung.*
[2] *Mud Volcano Research Center, Ministry of Public Works, Jl. Gayung Kebonsari No.50, Gayungan, Surabaya.*
[3] *Department of Geological Engineering, Pertamina University, Jl. Teuku Nyak Arief, Jakarta.*

* Corresponding author : : saepuloh@itb.ac.id, pamumpuni@itb.ac.id
Tel: +62 813-2024-2402; +62 813-2051-6627

Received:; Accepted:
DOI:

Abstract

Land subsidence in the Sidoarjo Mud Volcano (SMV) area has been widely recognized as a consequence of sustained mud discharge and progressive subsurface consolidation. Earlier geodetic studies using GPS and InSAR, combined with geological and geomechanical investigations, have demonstrated persistent long-term ground deformation, widespread flooding, and severe infrastructure damage linked to these processes. This study aims to (1) quantify spatial and temporal subsidence rates, (2) identify the dominant controlling mechanisms, and (3) estimate the relative contributions of fluid discharge and natural consolidation to total subsidence. Surface deformation was derived through time-series analysis of Sentinel-1A SAR data using the pair-wise logic technique differential interferometric synthetic aperture radar (PLT-D-InSAR). These results were integrated with one-dimensional (1D) consolidation modeling based on lithological coring data and mud discharge records.

The PLT-D-InSAR analysis successfully captured detailed subsidence patterns over a wide area and shows good agreement with GPS observations ($R^2 \approx 0.82$). The combined D-InSAR, consolidation, and discharge analysis reveals a very strong correlation ($R^2 \approx 0.97$), indicating that subsidence is mainly governed by fluid discharge and consolidation processes. Fluid discharge accounts for approximately 72.2% of the total subsidence, while natural consolidation contributes about 16.5%. The highest subsidence rates are concentrated near the mudflow center and are structurally influenced by the Watukosek and Siring faults. These findings highlight the dominant role of discharge-induced deformation and provide important constraints for long-term hazard assessment and land-use planning in the SMV region.

Keywords: Land subsidence, PLT D-InSAR, 1D consolidation, Sidoarjo mud

1. Introduction

Land subsidence caused by gas and fluid discharge from the ground in the exploration area of the Banjar Panji Well, Porong District, Sidoarjo Regency, East Java Province (Davids et al., 2007). Mud volcanoes are surface expressions of mud originating from the subsurface of the ground surface. The mud volcano topography depends on the channel geometry and the eruption material's physical properties, such as dome morphology, mud pie with low topography, or cones (Kopf, 2002). The primary cause of land subsidence in Sidoarjo is the continuous eruption of the Sidoarjo mud volcano, which began in May 2006. This eruption has led to the collapse of the overburden due to the removal of subsurface material (Abidin et al., 2009). The area's geological structure contributes to the subsidence, including fault and sediment contribute land subsidence. The geological structure in this area is controlled by a regional compressional tectonic regime associated with the convergence of the Indo-Australian and Eurasian plates. This setting has led to the development of pre-existing fault systems, including the Watukosek Fault (Tingay, 2015). The Watukosek Fault System, in particular, has played a role in the deformation observed in the region (Yulyta et al., 2016).

Mud volcano occurs along with the material discharge in rocks, liquids, or gases from rock formations at depths with overpressure conditions, forming a distinctive morphology (Stewart & Davies, 2005). Previous studies reported the mud volcano's characteristics, including the surface morphology, material types, and discharge process (Burhannudinnur, 2016). Sidoarjo Mud Volcano, termed SMV, is one of the mud volcano phenomena often found in the northern part of Java Island, explicitly formed in the eastern Kendeng Zone (Fig.1).

As reported by previous studies, the extruded materials from mud volcanoes can cause land subsidence because land subsidence has occurred in specific areas, such as unstable areas. Land subsidence may originate from excessive groundwater exploitation, massive discharge of gas and mud from the ground to the surface, the load of buildings above the surface, natural consolidation of ground layers, and tectonic forces (Abidin et al., 2009). According to Istadi et al. (2018), land subsidence can occur locally and regionally due to natural and subsurface subsidence.

Natural subsidence is caused by geological processes such as volcanic and tectonic activities, geological material, and subsurface fractures. Subsurface subsidence is caused by fluid discharge below the surface, such as groundwater or oil and gas (Rateb & Abotaleb, 2020).

The SMV is geologically located in the back-arc basin near the volcanic arc presented by the Mts. Penanggungan and Arjuno-Welirang (Fig.1). In addition, the SMV main eruption center is located in the lineament of the Watukosek Fault System, oriented Southwest – Northeast (Fig.1). According to the geological setting, the large amount of mud discharge, the high temperature, and the gas content, a previous study reported that the Sidoarjo mud volcano phenomenon is also related to the southern part's volcanic activity (Manzini et al., 2018). Their studies were supported by the helium isotope composition of the Lusi mud volcano fluid, which is remarkably similar to the Welirang volcanic fluid, indicating the presence of magmatic gas (MVMC, 2022).

A study about land subsidence with differential interferometric synthetic aperture radar (D-InSAR) has been done by Abidin et al. (2009). Their method can determine either medium, low, or high land subsidence values, thus identifying the affected areas within these zones in SMV. According to Wesley et al. (2010), consolidation only happens in clay and silt materials cause occurs in clay and silt materials due to their fine-grained nature. These materials have small particle sizes and low permeability, which cause them to compress and settle over time under the influence of a load. Based on (Supandjono et al., 1992) regional geological map, the SMV area is dominated by alluvial surface deposits, which consist of a mixture of sand, silt, clay, and gravel. The consolidation process involves expulsing water from the pores of these soils, leading to a decrease in volume and an increase in soil density. This is in contrast to coarser-grained materials like sand and gravel, which have higher permeability and drain more quickly, reducing the extent of consolidation (Tingay, 2014).

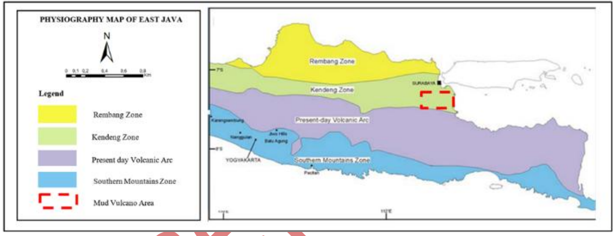

Fig. 1. Map Location of Sidoarjo Mud Volcano (SMV) at physiography of East Java presented by red square and overlaid on the Kendeng zone and present-day volcanic arc (Sudarsono & Sudjarwo, 2008).

Abidin et al. (2009) also studied land subsidence using the D-InSAR method. This method can determine the subsidence value (m/year) that occurred during the 2 years since the first eruption of Lusi. The D-InSAR approach monitors changes in land elevation with high spatial and temporal resolution. Meanwhile, land subsidence using the 1-dimensional (1D) consolidation method was conducted by Achmad Taufiq (2023) in the Bandung basin. This study presents a detailed analysis of the rate of natural consolidation subsidence and the rate of subsidence of fluid release from the subsurface. By comparing these parameters, this study aims to determine whether land subsidence at a particular location is caused by natural consolidation or the influence of fluids.

We analyzed land subsidence rates derived from D-InSAR, natural consolidation, and fluid-related processes. These parameters are compared using the coefficient of determination (R^2) to assess the performance of the linear regression model in explaining subsidence variability. Higher R^2 values indicate a better model fit. Beyond statistical assessment, the analysis aids in identifying the dominant factors controlling land subsidence in the study area.

2. Data and Methods

2.1 Data

Sentinel-1 Single Look Complex (SLC) level-1 product, containing phase and amplitude data, is used in this research to obtain the rate of land subsidence. The Sentinel-1 satellite captured the radar images for each observation time. The spatial resolution of Sentinel-1 about 5 m produces excellent morphological detection despite bad weather conditions (Yamaguchi, 1985). To reduce the line of sight (LOS) distortion, two orbits of Sentinel-1 data in ascending and descending were combined to obtain a high contrast from both sides (Saepuloh et al., 2022). To obtain the monthly average subsidence rate, the twelve Sentinel-1 data for each month from 2016 to 2023 are used by selecting the VV polarization type in the C-band. Table 1 provides a detailed list of the Sentinel-1 data used in this study. The GPS subsidence rate data from the Mud Volcano Monitoring Center (MVMC), consisting of 10 monitoring points, were used to validate the deformation results.

Table 1. Table title should be placed above the table and adjust text to table width.

No	Data Pairs	Temporal Baseline (Daily)	Pair	Pair-Wise	
	Ascending:		1		
1	January – February	28		I	
2	February – March	29	2		
3	March – April	29	3	III	II
4	April – May	26	4		
5	May – June	27	5	V	IV
6	June – July	27	6		
7	July – August	26	7	VII	VI
8	August – September	28	8		
9	September – October	28	9		VIII
10	October – November	26	10	IX	
11	November – December	27	11		X

The 1D consolidation was calculated through the core of boreholes to obtain subsurface lithology. Lithological cross-sections were developed using borehole correlation and stratigraphic interpolation. The lithological parameters used in this study were obtained from laboratory test results compiled in the MVMC (2022) dataset, provided by the Sidoarjo Mud Volcano Monitoring Center under the Ministry of Public Works and Housing (PUPR).

The data consist of 10 boreholes with a depth of approximately 30 m, including parameters such as saturated unit weight, dry unit weight, void ratio, compression index (Cc), and coefficient of consolidation (Cv). These parameters were used to estimate natural consolidation and fluid discharge in the study area. Table 2 provides a detailed list of the borehole data used in this study, while the spatial distribution of the boreholes is shown in Fig. 6.

Tabel 1. list of the borehole data used in this study.

Borehole	Depth (m)	Soil type	Moisture unit weight (kN/m3)	Dry unit weight (kN/m3)	Consolidation parameters		
					Void Ratio	cc	cv (cm^2/s)
	7.5 - 8.0	Sandy Clayey Silt	18.2	14.18	0.81	0.55	0.0489
BH 1	21.50-22.0	Sandy Clayey Silt	17.5	12.65	1.02	0.33	0.047
	25.50-26.00	Clayey Silt	14.2	7.19	2.45	0.63	0.0454
	13,50 - 14,00	Clayey Silty Sand	-	-	-	-	-
BH 2	17,50-18,00	Clayey Silt	14.10	7.31	2.29	0.73	0.0267
	21,50-22,00	Silty Clay	13.90	6.71	2.65	0.84	0.0392
	15,50 - 16,00	Silty Clay	20	17	3.41	0.78	0.0181
BH 3	19,50 - 20,00	Clayey Silt	20	17	2.82	0.54	0.0161
	23,50 - 24,00	Silty Clay	20	17	3.23	0.56	0.0468
	17,50 - 18,00	sandy, clayey silt	14.1	7.31	2.29	0.52	0.0417
BH 4	21,50 - 22,00	sandy, clayey silt	15	8.21	2.19	0.61	0.0457
	25,50 - 26,00	clayey silt	13.5	7.02	2.74	0.89	0.0422
	09,50 - 10,00	clayey silt	14.8	8.62	1.79	0.39	0.0542
BH 5	15,50 - 16,00	clayey silt	14.6	8.62	1.79	1.13	0.0262
	17,50 - 18,00	sandy, clayey silt	14.3	7.52	2.24	0.63	0.0491
	03,50 - 04,00	clayey sandy silt	17.6	12.9	0.99	0.52	0.0523
BH 6	11,50 - 12,00	clayey sandy silt	16.3	11.4	0.72	0.84	0.0114
	19,50 - 20,00	gravely clayey silt	9.2	9.22	0.81	0.67	0.0484
	03,50 - 04,00	clayey sandy silt	17.6	12.9	0.99	0.84	0.0523
BH 7	11,50 - 12,00	clayey sandy silt	16.3	11.4	0.72	0.67	0.0484
	19,50 - 20,00	gravely clayey silt	9.2	9.22	0.81	0.52	0.0114
	03,50 - 04,00	Sandy Silt	14.2	11.3	0.97	0.63	0.04873
	11,50 - 12,00	Clayey Silt	12.2	11.8	0.84	0.88	0.03117
BH 8	19,50 - 20,00	Clayey	10.22	9.2	0.91	0.77	0.0584

2.2 Methods

2.2.1 D-InSAR Method

The D-InSAR processing requires SAR data pairs at the SLC level with the same footprint but different acquisition times (Saepuloh et al., 2018). -First, the image pair was registered to reposition the slave image pixel and match the master image pixel with subpixel accuracy. Second, the Master and the Slave Images were merged by back geocoding to determine the pixel position reference of the image using DEM. Third, the bursts were combined using the deburst process and interferogram settings. This was because each burst's split and cogging results were still separated. The topographic Phase Correction Process was conducted to obtain a model that corrected the initial interferogram. This stage is the differentiator between ordinary D-InSAR and In-SAR processing. Subsequently, the filtering process significantly reduced speckle noise in interferogram images, corrected topographically. A multi-looking Process was used for data compression in SLC format to increase the focus of the image in pixel range and azimuth, thereby increasing the radiometric resolution. The terrain correction process was conducted to facilitate the change to a planimetric coordinate system. This process is performed to correct the distortion of the image geometry in the slant coordinates into the ground range geometry (Hongdong et al., 2011).

The earth surface changes were determined from D-InSAR phase data change. The formed phase changes, as shown in the interferogram imagery, contain the contribution of several phases reported by (Hanssen, 2001):

$$\Phi_{int} = \Phi_{topo} + \Phi_{defo} + \Phi_{orb} + \Phi_{atm} + \Phi_{noise} \qquad (1)$$

Where:
Φ_topo = Phase difference between two SAR images
Φ_defo= Topography phase as a reference
Φ_orb = Orbit phase
Φ_atm = Phase of atmospheric influence
Φ_noise= Phase of noise influence

To produce more accurate values, the pairwise logic technique (PLT) D-InSAR technique is used with an external Digital Elevation Model (DEM) from SRTM by giving precise elevation information that can be used to match the radar data with the actual earth surface into radar coordinates and scaling 1: 25.000 using a baseline (Massonet, 1998). By giving precise elevation information from DEM that can be used to match the radar data with the actual Earth's surface, a DEM aids in correcting these aberrations. This process produced a subsidence rate from D-InSAR, has a high-quality rate by DEM and aids in correcting these aberrations. (Saepuloh et al., 2022). It can be seen in Fig.2 that the PLT was applied to the D-InSAR interferogram to minimize the atmospheric phase delay using everyday image pair (Fig.2).

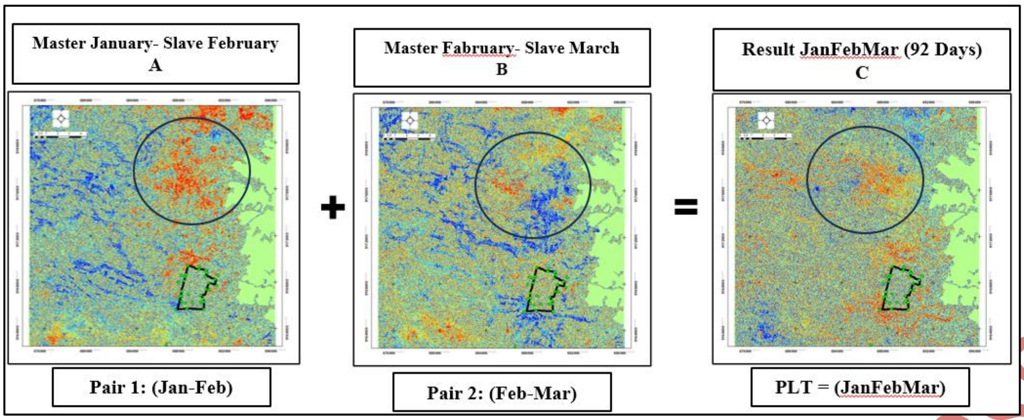

Fig. 2. Illustration of Sentinel 1A PLT D-InSAR process to reduce atmospheric phase delay. (A) Master (January) – Slave (February) (B) Master (February) – Slave (March) (C) Result PLT. The red circle shows the noise correction process in the study area.

2.2.2 1D consolidation Method

Terzaghi (1925) introduced the theory of 1D consolidation rate. The subsidence magnitude in a certain period, known as the degree of consolidation, was needed to determine the subsidence time. Ht value became half the thickness of the layer due to the permeability of the layer underneath. However, it remains unchanged when the layer below is not permeable. The relationship between the degree of consolidation (U) and time factor (Tv) was used to determine the consolidation duration (Sarah et al., 2023).

In natural consolidation, the process of reducing sediment or material volume occurs due to the burden of the above layer (gravitational compaction). It was essential to acknowledge that the gravitational compaction or the overburden caused the underlying sediment layers to be compacted due to the release of excess pore pressure and the contact rearrangement between grains (Skempton, 1969). Hydrostatic pressure analysis was conducted to determine the influence of fluid parameters. The calculated pressure was experienced by the fluid, causing measurable land subversion. In geotechnics, hydrostatic pressure is essential in calculating soil overburden because it can affect soil stability and deformation (Tingay, 2015).

Analytical methods for 1D consolidation equations 2, under various subsurface conditions, have been developed, allowing accurate predictions for different types of boreholes. According to Stickle and Pastor. (2018) This method can calculate vertical stress (Δp) and effective stress (p_0) in equation 2 was conducted using the dry density (γ) and wet density (γ) components in the study area. The void ratio (e_0), compression index (Cc), and consolidation coefficient (Cv) components are used to calculate the maximum subsidence value. The calculation of land subsidence due to maximum consolidation is carried out by the 1D consolidation concept of Terzaghi as follows:

$$Sc = \frac{C_c H}{1+e_0} \log\left(\frac{p_0+\Delta p}{p_0}\right) \qquad (2)$$

Where:

Sc = subsidence due to primary consolidation,
Cc = compression index,
H = clay thickness,
e_0 = an initial void ratio,
p_0 = effective stress and
Δp = vertical stress over the clay layer (Das, 2010)

The subsidence time determination requires the magnitude of decrease in a certain period called the degree of consolidation. The relationship between degree of consolidation (U) and time factor (TV) was used to find the consolidation time (t) using Equation 3 as follows:

$$T_v = \frac{C_v t}{{H_t}^2} \qquad (3)$$

From these two analyses between D-InSAR and 1D consolidation, this study has a subsidence rate in the same borehole area. The annual average subsidence rate can be obtained, which is then analyzed and validated in the exact location with field survey validation to determine the correlation between the existing subsidence rate and subsurface geological conditions. After knowing the subsidence rate from DinSAR and 1D Consolidation, an interpolation was carried out to determine the value in the distribution of locations without borehole data.

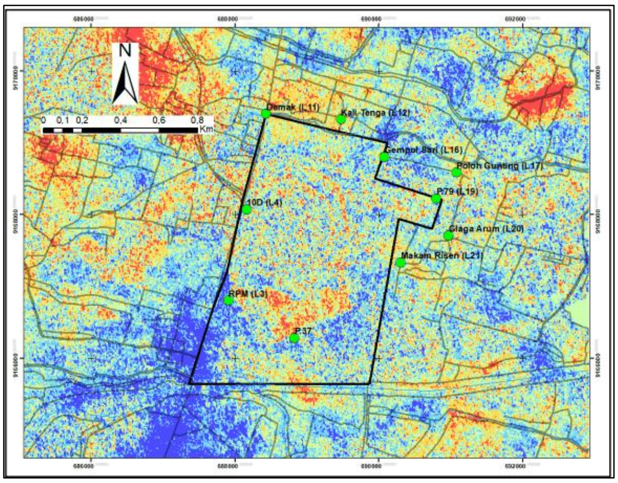

Fig.3. The D-InSAR interferogram presents total subsidence in 8 years overlaid by field observation points (squared greens) measurements at the study area.

3. Result

3.1 Land subsidence based on D-InSAR and GPS Validation

Differential Interferometric Synthetic Aperture Radar (D-InSAR) is a powerful technique used to measure ground deformation, including land subsidence, with high precision. D-InSAR processing from the Sentinel Application Platform (SNAP) was obtained using 96 Sentinel 1A (Ascending) data, resulting in a decreased value for 8 years. The results of the Master and Slave image processing from 2016 to 2023 yearly can be seen in Figure 3. The results of D-InSAR processing in SMV have a value range of 0 – 10.50 cm, indicating uplift deformation spread in the southern region and subsidence of 80.57 – 116.51 cm spread across the northern region. Location P37 has the highest subsidence value of 2.13 cm/year, as seen in Table 3. Compared to other observation points, the high subsidence value of P37 is due to the location close to the center of the SMV.

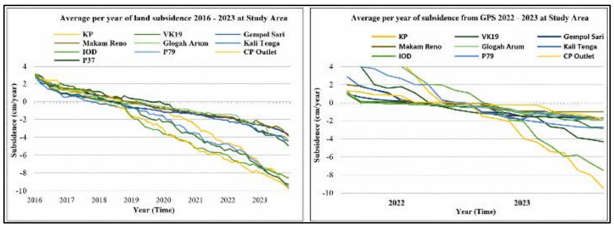

Fig.4. The temporal subsidence of ground surface obtained by D-InSAR processing from 2016 to 2023 (A) and global positioning system (GPS) measurements from 2022-2023 (B).

The results of D-InSAR processing in 2016-2023 show the yearly subsidence rate. The data is then compared with GPS data obtained based on MVMC (2022) in 24 months of measurement from 2021-2022 (Fig.4). The results can be seen in the 10 boreholes. Significant land subsidence is located at the P37, Rpm, and Cp Outlet locations compared to the map in Fig.3. The location is in a zone with a high level of land subsidence.

3.2 Land subsidence rate based on D-InSAR and GPS Validation

Land subsidence in the Sidoarjo Mud Volcano (SMV) area was analyzed using time-series Sentinel-1A D-InSAR data acquired from 2016 to 2023, complemented by GPS observations from 10 monitoring points distributed across the study area. The GPS data were processed relative to fixed reference stations to obtain displacement magnitude and direction.

The D-InSAR analysis shows a consistent subsidence pattern with rates ranging from 0.5 to 2.1 m/year (Fig. 4). Meanwhile, GPS measurements for the 2022–2023 period indicate subsidence rates of 0.9 to 2.2 m/year (Table 3). The comparison between D-InSAR and GPS results demonstrates good agreement in both magnitude and spatial pattern, confirming the reliability of D-InSAR for large-scale deformation monitoring, while GPS provides essential ground-based validation.

Table 3. Average deformation rate obtained by D-InSAR and GPS measurements

No	Location	Coordinate		D-InSAR subsidence rate (cm/year)	GPS subsidence rate (cm/year)
		Latitude	Longitude		
1	Poloh Gunting	7°31'05.65909"S	112°43'54.14"E	1.44	1.30
2	Gempol Sari	7°30'58.74438"S	112°43'21.36"E	1.66	1.44
3	Kali Tenga	7°30'41.81950"S	112°43'01.66"E	1.02	1.46
4	Makam Reno	7°31'46.62230"S	112°43'28.92"E	0.56	0.93
5	Glaga Arum	7°31'34.39290"S	112°43'50.51"E	1.26	1.20
6	P.79	7°31'17.50648"S	112°43'45.06"E	2.12	2.15
7	P.37	7°32'21.01236"S	112°42'40.86"E	2.13	2.20
8	RPM	7°32'04.13824"S	112°42'10.83"E	1.29	1.31
9	10D	7°31'22.75570"S	112°42'18.89"E	1.84	1.90
10	Demak	7°30'39.39341"S	112°42'27.54"E	1.57	1.73
		Subsidence rate/year		1.56	1.49

Table 4. Subsidence rate based on D-InSAR at borehole locations.

No	Location	Coordinate		D-InSAR Subsidence Rate	Average Subsidence Rate (Total)	Average Subsidence Rate (Natural)	Average Subsidence Rate (Fluida)
		Latitude	Longitude				
1	BH 1	7° 31' 12.42" S	112°43' 11.5" E	1.44	1.25	0.39	0.86
2	BH 2	7° 31' 6.1" S	112° 43' 21.1" E	0.66	0.66	0.13	0.52
3	BH 3	7° 31' 8.27" S	112° 43' 26.2" E	2.02	2.26	0.58	1.67
4	BH 4	7° 30' 49.55" S	112° 42' 52.8" E	0.56	0.50	0.20	0.30
5	BH 5	7° 30' 45.48" S	112° 42' 46.2" E	1.16	1.00	0.26	0.74
6	BH 6	7° 30' 39.27" S	112° 42' 28.1" E	0.91	0.67	0.37	0.30
7	BH 7	7° 31' 39.95" S	112° 42' 14.4" E	2.83	2.78	0.43	2.35
8	BH 8	7° 32' 17.77" S	112° 42' 50.9" E	2.89	2.82	0.47	2.35
		Subsidence rate/year		1.56	1.49	0.35	1.13

3.3 Analysis of land subsidence rate D-InSAR and GPS with R² correlation

This A correlation analysis was conducted to validate the D-InSAR deformation results against GPS measurements obtained from the Mud Volcano Monitoring Center (MVMC), consisting of 10 monitoring points. The comparison was performed using the average subsidence rates derived from D-InSAR time-series data (2016–2023) and GPS observations for the corresponding locations. A scatter plot was used to evaluate the relationship between the two datasets (Fig. 5). The results show a good agreement, with a coefficient of determination (R^2) of approximately 0.82, indicating that the D-InSAR-derived deformation is consistent with in-situ GPS measurements and can be reliably used for further analysis.

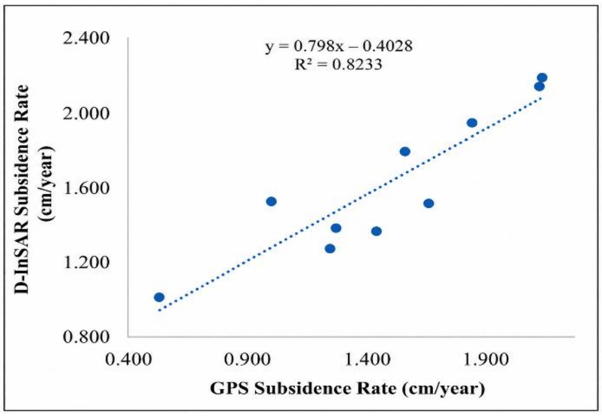

Fig.5. Correlation of deformation obtained from D-InSAR and GPS. The X and Y axes.

3.4 Analysis of land subsidence due to 1D consolidation (natural consolidation and fluid discharge)

Fluid discharge and natural consolidation factors all play a role in determining the maximum subsidence (Tingay, 2015). Equations 1 and 2 of the Terzaghi analysis were used to determine the value of land subsidence produced from those factors. The Consolidation 1D can describe subsidence calculation and predict the time needed to obtain maximum subsidence. The subsidence rate of D-InSAR deformation in 2016-2023 must compared to the 1D consolidation in the exact location to know the correlation between the two methods. The result from two methods between 1D consolidation and D-InSAR correlates with R^2= 0.96, which can be seen in Fig.7a. The comparison is needed to describe the subsidence condition without a subsurface calculation so that it can predict other locations.

The results showed that the total average subsidence of D-InSAR is 1.60 cm/year (Table 2). The total subsidence rate derived from the natural consolidation is 0,358 cm/year, and fluid discharge is 1.13 cm/year (see Table 2). This result refers to the borehole data in 8 locations (see Fig. 6), where the effect of fluid discharge is higher than that of natural consolidation. The areas in BH 7 and BH 8 have the highest subsidence values, where BH 7 has a total average subsidence rate of 2.83 cm/year, and BH 8 has a total average subsidence rate of 2.89 cm/year (See Fig. 6 and Table 4).

The land subsidence from 1D Consolidation (natural consolidation and fluid discharge) at the BH 7 location has a subsidence rate of 2.78 cm/year, and BH 8 has a subsidence rate of 2.82 cm/year. However, the result has the smallest subsidence value at the BH 2 location of 0.66 cm/year and BH 4 at 0.50 cm/year (see Table 4).

The clay thickness analyzed in the study area influenced the natural consolidation parameter with the highest subsidence rate at BH 5 and BH 2. The geological properties of clay in BH 5 and BH 2 can cause a significant value and rate of land subsidence in this area. In addition to these factors, the more excellent layer thickness factor in this area significantly influences other regions (see Table 2). The land subsidence value can be seen partially because a maximum value is calculated from the natural consolidation and fluid discharge factors. Meanwhile, causes fluid discharge with the highest subsidence rate at BH 7 and BH 8 causes the content of the determining material in each drill, such as vertical stress and effective stress in equation 2, was conducted using the dry density (γ) and wet density (γ) components in the study area. The void ratio (e0), compression index (Cc), and consolidation coefficient (Cv) components have a smaller influence level than others.

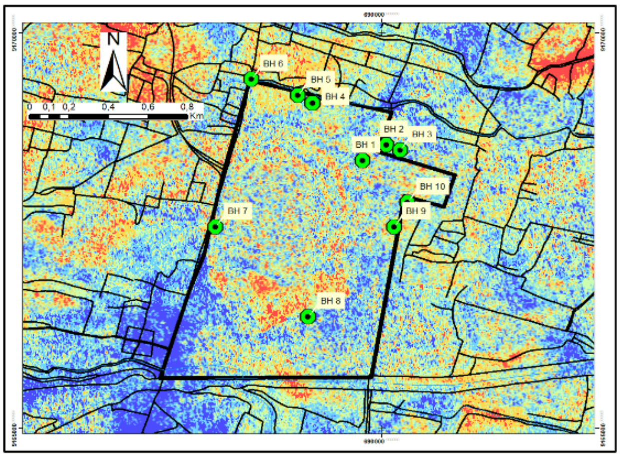

Fig.6. Deformation map shows accumulated subsidence in borehole locations presented by green circles overlaid with D-InSAR interferogram.

Under 90-percent consolidation conditions, the total land subsidence rate is between 0.50 and 2.82 cm/year (see Table 4). The result from Equation 2 and Equation 3 shows that BH 7 and BH 8 have significant values for compression index (Cc), consolidation coefficient (Cv), and void ratio (e0) compared to the others (see Table 1). The amount and level of substantial land subsidence at this location may be due to the lithology characteristics of clay. In addition to the elements mentioned above, the higher layer thickness of the area plays an extraordinary role compared to the embankment boundary. Volcanic deposits from the mud volcano eruption created volcanic fans with non-compressive lithological characteristics that impacted the embankment margins.

The fluid discharge parameter calculations showed the highest subsidence value at BH 7, about 2.35 cm/year, and subsidence value at BH 8, about 2.23 cm/year (Table 2). According to Tingay et al. (2015), land subsidence occurs because soil volume shrinks due to reduced adequate pressure. The mud eruption center near BH 7 and BH 8 is the cause of a as pore pressure increases and high-density water fills the pores of the soil, the soil can lose its strength and undergo compression, because, based on Table 2, there are materials such as silt and clay that are easily compressed.

According to equation 3 in eight locations, shown in Figure 7a and Figure 8b, the maximum subsidence due to natural consolidation and the estimated time of subsidence from 2016 onwards will end on 762 to 3472 years since 2016 with a total subsidence maximum from 100 cm to 700 cm. However, subsidence caused by fluid discharge has a period of from 2000 to 4000 years since 2016.

3.5 Correlation of D-InSAR, Natural Consolidation, and Fluid Discharge

By integrating D-InSAR deformation with natural consolidation and fluid discharge from the subsurface boreholes data, the interaction between fluid dynamics and soil deformation can be obtained that 1D consolidation caused by natural consolidation and fluid discharge. The correlation data in Figure 7 describes the coefficient between 1D consolidation and D-InSAR as high as about. R^2 = 0.96, indicating that D-InSAR, the data can be used to find out qualitatively with a spatial approach to locations with higher, medium, and lower levels of land subsidence. The correlation coefficient between 1D consolidation and natural consolidation was low about R^2 = 0.359, indicating that natural consolidation has less effect because the calculation is based on the natural load caused by the previous layer (Das, 2010). The correlation coefficient between D-InSAR and fluid discharge was high about R^2= 0.972, it is influenced by the Compression Index (Cc), Void Ratio (e_0), and Consolidation Coefficient (Cv) (Sarah et al., 2023). According to Equation 2, the subsidence rate from fluid discharge has contributed about 72.2% and natural consolidation has contributed about 16.5% of total subsidence in SMV. The results explain that fluids affect land subsidence in Sidoarjo Regency because the volume of fluid discharge in the mud volcano is also high intensity and affects consolidation.

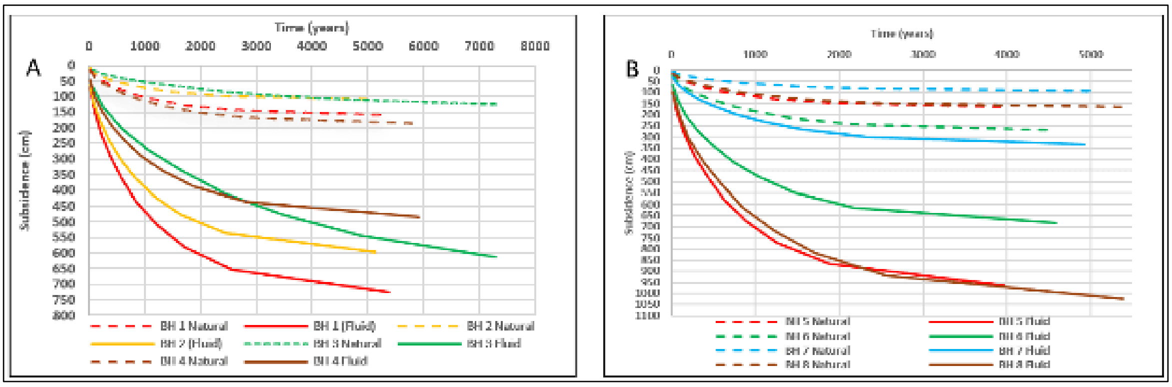

Fig.7. Comparison of the subsidence between natural consolidation and fluid discharge at BH 1–BH 4 (A) and BH 5–BH 8 (B).

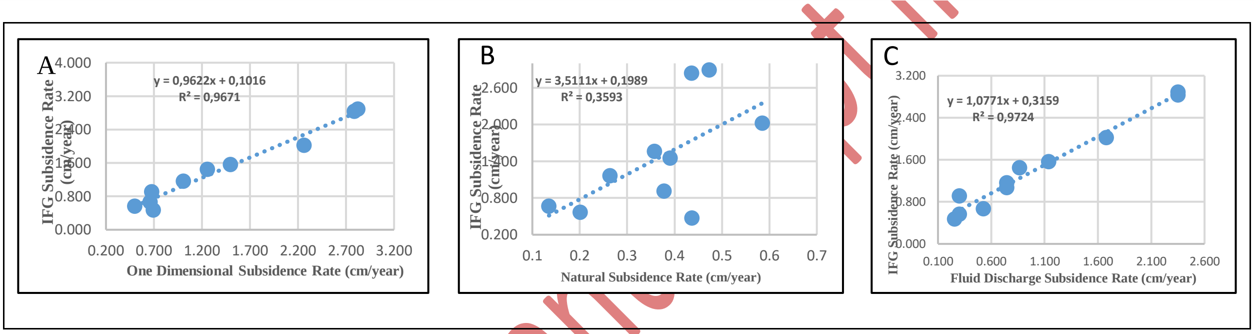

Fig. 8. A comparison of the subsidence rate based on D-InSAR and total 1D consolidation (A), D-InSAR and natural consolidation (B), as well as D-InSAR and fluid discharge rates (C).

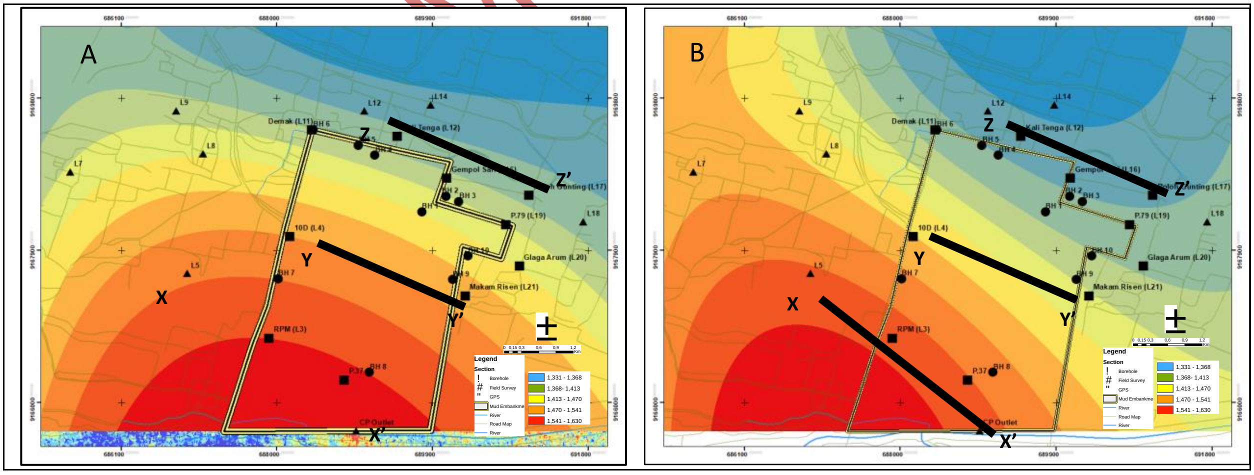

Fig. 9. The subsidence rate map based on total 1D consolidation (A) and fluid discharge (B).

3.6 Subsidence rate map based on total 1D of D-InSAR, Natural Consolidation, and Fluid Discharge

The subsidence rate map based on total 1D consolidation shows the level of contribution between natural consolidation and fluid discharge that has different impacts at each location. Based on the subsidence rate map based on total 1D results, locations in red have high subsidence values about 1.47 – 1.83 cm/year, yellow have moderate subsidence values about 1.36– 1.47 cm/year, and blue have low subsidence values about 1.01 – 1.36 cm/year. The subsidence rate map based on a total 1D map has a total value range of 0.33 - 2.6 cm/year. The subsidence rate map based on total 1D analysis results shows that the southern region had a higher subsidence value than the northern region; the value was influenced by the more significant fluids content on the location (P37, CP Outlet, BH7, and BH8).

A subsidence rate map based on total 1D is used to predict values in areas not covered by the observation and sampling locations. The values around the location studied influence the subsidence rate map based on the total 1D value. The subsidence rate map is based on a total 1D model. In this study, Equation 3 with R^2 about 0.96 is used to obtain a total of 8 data, and Equation 3 with R^2 about 0.97 is used to obtain fluid discharge data. The results of the subsidence rate map based on total 1D using kriging shows the analysis of the highest subsidence rate in red, whereas the results of the lowest subsidence rate are in blue. The observation locations at the Cp Outlet, P37, Rpm, and BH 8 have the highest subsidence rate, about 1.29 to 2.13 cm/year, whereas BH 4 and BH 6 have the lowest subsidence rate of about 0.56 to 0.91 cm/year. The difference in the subsidence hazards can be seen clearly in the interpolated subsidence rate map based on equations 2 and 3 (Fig.9).

4 Discussion

4.1 High subsidence areas (1.47 – 1.83 cm/year)

Based on the total 1D analysis results, the subsidence rate map illustrated that the anomalies could be significantly red at locations around the mud volcano crater. Fluid discharge significantly contributes to land subsidence at L9, P37, BH 7, and BH 8 locations. The discharge of fluids in the form of water, gas, and mud around the location causes a reduction in fluid pressure; hence, the reservoir rock compacted because the weight of the rock above it begins to press harder (Tingay, 2015). Rock grains in the reservoir move closer together, reducing the total volume and causing subsidence at the surface (Sarah, 2023). At the BH 7 and P37, soil samples were observed, and it was found that the soil pH was 5.5, very acidic. According to Kopf (2022), the acidic soil pH can accelerate the erosion process of rocks and other geological materials. Whereas the temperature measured is 36.4°C, the humidity level is 3.33% RH. Apart from the fluid discharge, land subsidence can also occur due to loads on the ground surface, such as buildings (Terzaghi, 1943). At location L9, a building experienced subsidence, proven by direct measurement using a ruler, showing subsidence of 27 cm (Fig. 10).

The subsurface geological conditions along the X–X' section (Fig. 11) were constructed based on lithological correlation of borehole data obtained from BH7 and BH8. The cross-section was generated by interpolating lithological layers between boreholes using stratigraphic correlation to represent the spatial distribution of subsurface materials. Based on the correlation results, locations L9, P37, BH 7, and BH 8 are dominated by silt and clay materials, with the thickness of silt ranging from 2 to 19 m. Silt and clay materials cause land subsidence more quickly than in other locations. The distribution of silt material can be seen from the anomaly as seen in the subsurface lithology, and there is also an alternation between silt and clay with a layer thickness of 2 - 9 m. Lithological variability plays a significant role in controlling the spatial variation of land subsidence in the study area.

Fig.10. Field verifications at the study area, Sidoarjo Mud Volcano: BH 7 (A); L9 (B); and P37 (C). The locations of the photographs are depicted in Figure 8.

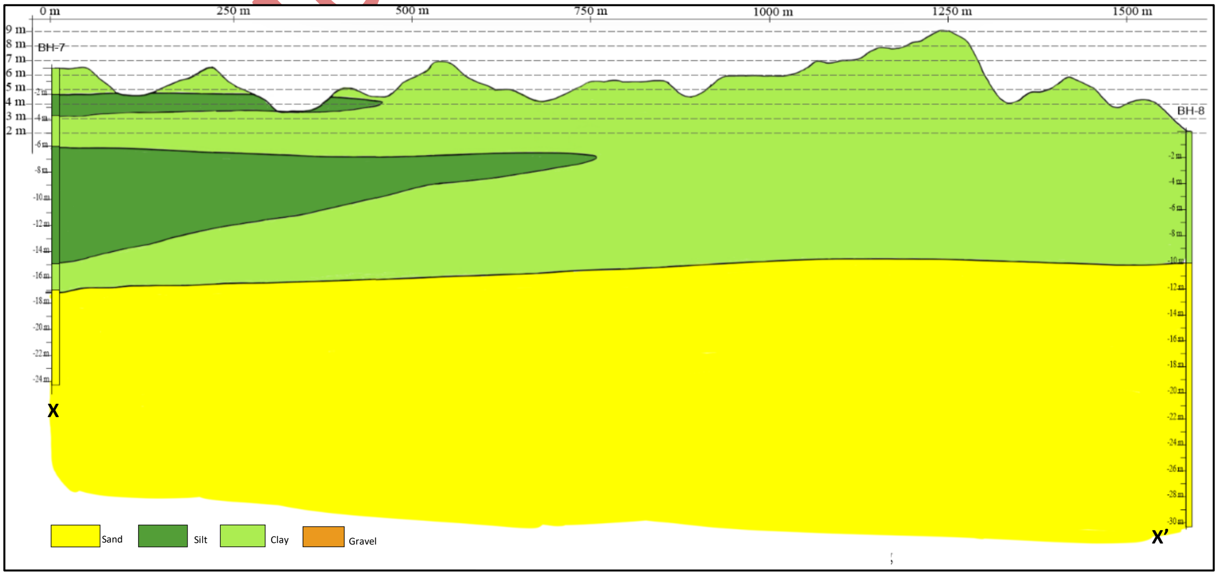

Fig. 11. Cross section line X – X' shows subsurface lithological in high subsidence area. The locations of sections X – X' are depicted in Figure 9.

4.2 Moderate subsidence areas (1.36 – 1.47 cm/year)

Subsidence rate maps based on total 1D results with moderate subsidence values are found at locations L5, L8, and P79. Field verification results in observation points L5 – L8 showed cracks in several buildings in the area (L9), whereas areas L8 and P79 showed a subsidence of around 10 - 18 cm measured by the ruler, as seen in Figure 12.

The results of these observations validated the subsurface geological conditions that can be seen in Fig.13 for Y – Y'(see Fig. 9). It shows that the area consists of a thick layer of clay, which, compared to other lithologies in the study area, can easily experience compaction and deformation when the pressure decreases. The cross-section showed that the clay material has an average thickness of 2-10 m and is relatively closer to the surface than silt, whereas the sand material has an average thickness of 3-16 m. Gravel and boulder inserts are also present, with a 1-3 m thickness.

Fig. 12. Field verifications at the study area on Sidoarjo Mud Volcano: L5 (A), L8 (B), and P79 (C). The locations of the photographs are depicted in Figure 9.

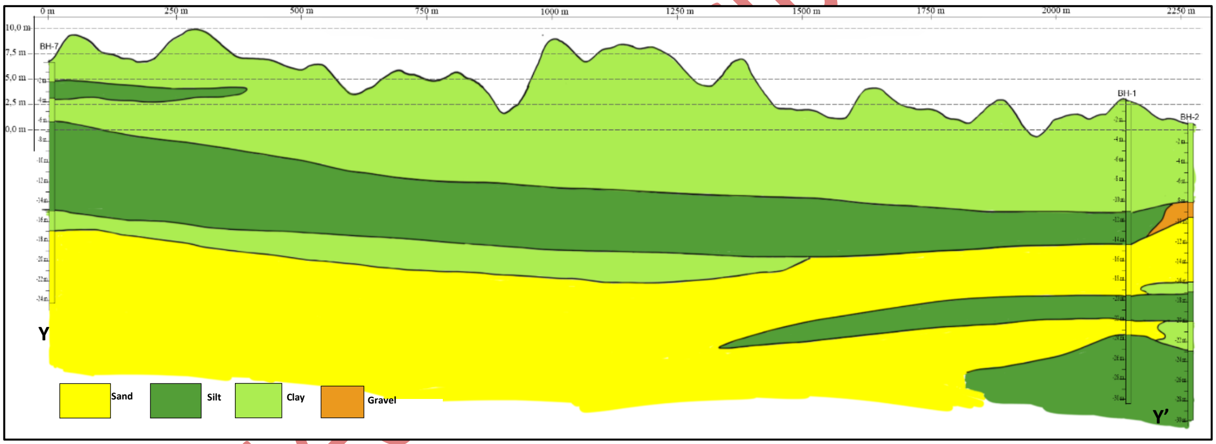

Fig. 13. Cross section line Y – Y' shows subsurface lithological in moderate subsidence area. The locations of sections Y – Y' are depicted in Figure 9.

Fig. 14. Field verifications at the study area, Sidoarjo Mud Volcano: L12 (A), L18 (B), and P79 (C). The locations of the photographs are depicted in Figure 8.

4.3 Low subsidence areas (1.01 – 1.36 cm/year)

Land subsidence with horizontal movements can change the slope or gradient of a river. If the land subsidence happens around the river, the gradient can become gentler, slowing the water flow, as seen in Fig.14 (L18). At this location, changes in topography can be seen, thereby increasing the risk of flooding. Some parts of the river that experience land subsidence also experience an increase in flow capacity. In contrast, others may experience a decrease in flow capacity, increasing the risk of flooding at the location (L12). Meanwhile, land subsidence with a vertical shift can be seen at P79; from field observation results, it is known that (P79) experienced subsidence of 19 cm.

The results of these observations validated the subsurface geological conditions that can be seen in Fig. 15 for Z – Z'(see Fig. 9). The subsurface geological condition in the Z – Z' cross section is dominated by silt and clay materials. Silt material has an average 2-10 m thickness and is relatively closer to the surface than clay. Clay material has an average thickness of 3-16 m. The cross-section also identifies the presence of sand gravel and boulder inserts.

Fig. 15. Cross-section line Z – Z' shows the subsurface lithological area in a low subsidence area. The locations of sections Y – Y' are depicted in Figure 9.

4.4 Influence of the Watukosek and Siring Faults

The mud volcano area is in the volcanic arc and back-arc basin complex, causing the high-temperature fluids to escape to the surface through weak zones in the form of faults or fractures caused by the formation of new faults and the reactivation of old faults (Stickel & Pastor, 2018). There are two active faults across the mud volcano eruption area: the Watukosek and Siring faults, which trend northeast-southwest, and the Siring fault, which trend northwest-southeast. These two faults are the conduits through which static magma fluid can be generated. These two active faults can cause a land subsidence area, also known as the area of influence (Mazzini et al., 2018). Continued fault activity could weaken the area's geological structure, making it more susceptible to subsidence and mudflows when additional disturbances such as drilling occur. Watukosek and Siring fault activity can cause changes in ground pressure. Fault movement can lead to the release of tectonic stress, which increases pore pressure in rock formations. Increased pore pressure can cause the land to release mud and water (Tingay, 2015).

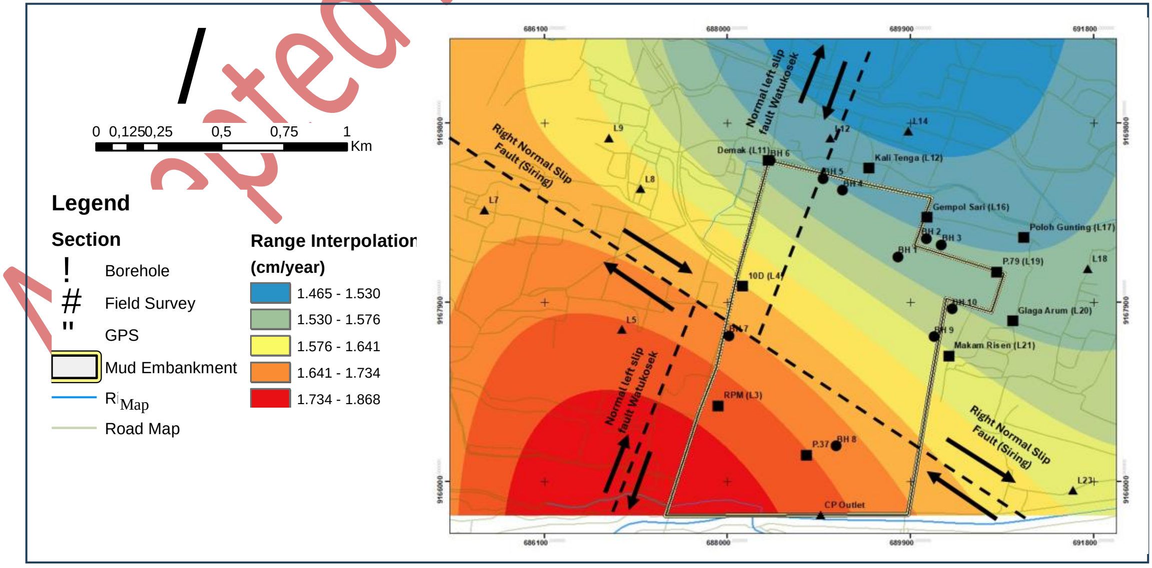

Fig. 16. A map illustrating the position of the faults overlaid on the map. The fault lines were presented by dashed lines with their movement direction (black arrows).

Subsidence in the central eruption area shows the fastest subsidence rate compared to the west of the central eruption or the Sidoarjo area and its surroundings. The central eruption area experienced the fastest subduction rate due to its significant release of fluid and gas. Meanwhile, progressive evolution uplift occurs east of the eruption center. Subsidence to the west of the eruption center has a long axis trending northeast-southwest, which aligns with the direction of the Siring Fault. In contrast, subsidence to the west of the eruption center has a long axis trending north-east-southwest, aligning with the Watukosek Fault's direction.

5. Conclusion

Time-series analysis of Sentinel-1A imagery using the pair-wise logic technique (PLT) D-InSAR demonstrates its capability to effectively monitor land subsidence over large areas, with strong agreement against GPS measurements (R^2 about 0.82). The integration of D-InSAR with 1D consolidation analysis and fluid discharge data further reveals a very high correlation (R^2 about 0.97), indicating that subsidence in the Lusi mud volcano area is primarily controlled by fluid discharge and natural consolidation processes. Fluid discharge contributes dominantly (72.2%) to subsidence, while natural consolidation accounts for 16.5%, with higher subsidence rates concentrated near the mudflow center and structurally influenced by the Watukosek and Siring faults.

This study contributes to the existing literature by providing a quantitative integration of remote sensing, geotechnical analysis, and hydrogeological factors to better explain subsidence mechanisms in mud volcano systems. However, the study is limited by the temporal resolution of satellite data, assumptions in 1D consolidation modeling, and the spatial distribution of ground validation points. Future research should incorporate longer time-series datasets, more advanced numerical modeling, and a denser monitoring network to improve the accuracy and understanding of subsidence dynamics.

Acknowledgements

The author would like to thank the Sidoarjo Mud Control Center for supporting the field survey by providing data and assistance facilities.

References

Abidin, H., Davies, R., Kusuma, M., Andreas, H., & Deguchi, T. 2009. Subsidence and uplift of Sidoarjo (East Java) due to the eruption of the Lusi mud volcano (2006–present). Environmental Geology, pp. 57, 833–844. https://doi.org/10.1007/S00254-008-1363-4.

Budiono, K., Handoko, H., Hernawan, U., & Godwin, G. (2010). Interpretation of subsurface geological structure in the Sidoarjo mudflow area based on ground penetrating radar (GPR) cross-section. Indonesian Journal on Geoscience, 5(3), 187–195. https://doi.org/10.17014/ijog.5.3.187-195

Burhannudinnur, M. and Noeradi, D. 2021. Understanding mud volcano system using Hele-Shaw (H-S) Experiment: Seismic confirmation at East Java Mud Volcano. Journal of Geoscience, Engineering, Environment, and Technology, 6(4), 206–216. https://doi.org/10.25299/jgeet.2021.6.4.7889

Davies, R. J., & Stewart, S. A. 2005. Emplacement of giant mud volcanoes in the South Caspian Basin: three-dimensional seismic reflection imaging of root zones. Journal of the Geological Society, 162(1), 1–4. https://doi.org/10.1144/0016-764903-078

Davies, R. J., Swarbrick, R. E., Evans, R. J., & Huuse, M. 2007. Birth of a mud volcano: East Java, 29 May 2006. GSA Today, 17(2), 4-9. https://doi.org/10.1130/GSAT01702A.1

Das, B. M. 2010. Principle of Geotechnological Engineering, 7th ed. (Seventh). Cengage Learning, USA, 688 p.

European Space Agency (ESA).2016. Sentinel-1 Satellite Description, htpps: sentinel. esa. int/web/sentinel/missions/

Hanssen, R.F. 2001. Radar interferometry: Data interpretation and error analysis. Kluwer Academic, Dordrecht, Boston. https://doi.org/10.1007/0-306-47633-9

Hongdong, F., Kazhong, D., Chengyu, J., Chuanguang, Z., & Jiqun, X. 2011. Land subsidence monitoring by D-InSAR technique. Mining Science and Technology, 21(6), 869–872. https://doi.org/10.1016/j.mstc.2011.05.030

Istadi, B., Pramono, G., Sumintadireja, P., and Alam, S. 2009. Modeling study of growth and potential geohazard for LUSI mud volcano: East Java, Indonesia. Marine and Petroleum Geology, 26, 1724-1739. https://doi.org/10.1016/J.MARPETGEO.2009.03.006.

Kopf, A.J. 2009. Significance of mud volcanism. Reviews of Geophysics,40(2). https://doi.org/10.1029/2000RG000093

Massonnet, D. and Feigl, K. L. 1998. Radar interferometry and its application to changes in the earth's surface. Reviews of Geophysics, 36(4), 441–500. https://doi.org/10.1029/97RG03139

Mazzini, A., Scholz, F., Svensen, H. H., Hensen, C., & Hadi, S. 2018. The geochemistry and origin of the hydrothermal water erupted at Lusi, Indonesia. Marine and Petroleum Geology, 90, 52–66. https://doi.org/10.1016/j.marpetgeo.2017.06.018

MVMC.2022. Mud vulcano data from Sidoarjo Mud Volcano Monitoring Center, Ministery Public Works, and Housing, data obtained through the ministry's internet site PUPR: https://sda.pu.go.id/publikasi/jurnal. It was downloaded on September 27, 2023.

Rateb, A. & Abotalib, A. Z. 2020. Inferencing the land subsidence in the Nile Delta using Sentinel-1 satellites and GPS between 2015 and 2019. Science of the Total Environment, p. 729. https://doi.org/10.1016/j.scitotenv.2020.138868

Saepuloh A, Sabrian P. G, and Fattah E.I. 2022: Pemrosesan Interferometric Syntetic Aperture Radar (Insar) untuk Eksplorasi dan Kebencanaan Geologi (Interferometric Synthetic Aperture Radar (Insar) Processing for Exploration and Geological Hazard). ITB Press, Bandung. (in Indonesian)

Saepuloh, A., Haeruddin, H., Heriawan, M. N., Kubo, T., Koike, K., and Malik, D. 2018. Application of lineament density extracted from the dual orbit of synthetic aperture radar (SAR) images to detect fluids paths in the Wayang Windu geothermal field (West Java, Indonesia). Geothermics, 72, 145–155. https://doi.org/10.1016/j.geothermics.2017.11.010

Sarah, D., Soebowo, E., Satriyo, N. A., Zulfahmi, and Wahyudin. 2023: Predictive Modelling of Land Subsidence Due to Groundwater Level Decline in Gedebage District, Bandung, Indonesia. IOP Conference Series: Earth and Environmental Science, 1227(1). https://doi.org/10.1088/1755-1315/1227/1/012016

Skempton, A. W. 1969. The consolidation of clays by gravitational compaction. Quarterly Journal of the Geological Society, 125(1–4), pp. 373–411. https://doi.org/10.1144/gsjgs.125.1.0373

Sudarsono, U. and Sudjarwo. B. S. 2008: Amblesan di daerah Porong Kabupaten Sidoarjo Jawa Timur (Subsidence in the Porong area, Sidoarjo Regency, East Java).

Jurnal Geologi Indonesia, 3, 1–9. (in Indonesian – English abstract available)

Stewart, S. A., & Davies, R. J. 2006. Structure and emplacement of mud volcano systems in the South Caspian Basin. AAPG Bulletin, 90(5), 771–786. https://doi.org/10.1306/11280505057

Stickle, M., & Pastor, M. 2018. A practical analytical solution for 1D consolidation. Géotechnique. https://doi.org/10.1680/JGEOT.16.P.268.

Supandjono, Santosa, S., dan Suwarti, T. 1992: Peta geologi lembar Malang, Jawa skala 1:100.000 (Geological map sheet of Malang, Java scale 1:100,000). Direktorat Geologi P3, Bandung. (in Indonesian)

Terzaghi, K. 1943. Theoretical soil mechanics. Wiley, New York.

Tingay, M.R.P., Rudolph, M.L., Manga, M., Davies, R.J., & Wang, C.Y. 2015. Initiation of the Lusi mudflow disaster. Nature Publishing Group, Nature Geoscience, 8(7), 493–494. https://doi.org/10.1038/ngeo2472

Yamaguchi Y .1985. Image-scale and look-direction effects on the detectability of lineaments in radar images Remote Sensing of Environment 17 117–27. https://doi.org/10.1016/0034-4257(85)90068-9

Yulyta, S. A., Taufik, M., and Hayati, N. 2016. Land subsidence detection using synthetic aperture radar (SAR) in Sidoarjo Mudflow area. In: Meilano, I., and Zulfakriza (Eds.), 5th International Symposium on Earthhazard and Disaster Mitigation: The Annual Symposium on Earthquake and Related Geohazard Research for Disaster Risk Reduction Article 060002 (AIP Conference Proceedings; Vol. 1730). American Institute of Physics Inc. https://doi.org/10.1063/1.4947408